International Forum on Aeroelasticity and Structural Dynamics
IFASD 2024
17-21 June 2024, The Hague, The Netherlands

POST-FLIGHT SYSTEM IDENTIFICATION AND AEROSERVOELASTIC MODEL UPDATING FOR PREDICTION AND VALIDATION OF THE ONSET OF FLUTTER

Özge Süelözgen[1], Gertjan Looye[1], Thiemo Kier[1], Matthias Wüstenhagen[1], Ramesh Konatala[1], Keith Soal[2], Nicolas Guérin[3], Bálint Vanek[4]

[1]German Aerospace Center DLR, Institute of System Dynamics and Control
Munchener Straße 20, 82234 Weßling, Germany
oezge.sueeloezgen@dlr.de

[2]German Aerospace Center DLR, Institute of Aeroelasticity
Bunsenstr. 10, 37073 Göttingen, Germany

[3]The French Aerospace Lab ONERA, Aerodynamics Aeroelasticity Acoustics Department
29 avenue de la division Leclerc, F-92322 Chatillon, France

[4]Institute for Computer Science and Control SZTAKI
Kende u. 13-17, 1111 Budapest, Hungary

Keywords: flight flutter testing, system identification, model updating, aeroelasticity, active flutter suppression, UAV

Abstract:

A validated aeroservoelastic (ASE) model allows, among other things, the extensive study of system performance and characteristics, the verification of analytical predictions, the support of flight envelope expansion during prototype testing, and the design of flight control laws. The ASE stability analysis is another crucial component of the configuration optimization and certification process over the intended operational envelope. In this context, the flutter phenomenon is a well-known example of a self-excited aeroelastic instability resulting from the interaction between unsteady aerodynamic forces and structural vibrations. The investigation of flutter through flight flutter testing is an essential part of aircraft certification. Significant amplitudes of vibration can be induced, eventually resulting in the structure's catastrophic failure. Instabilities have been derived that exceed well beyond the basic bending-torsion flutter into complex mechanisms involving ASE dynamics. With the guidance of accurate ASE models, a reliable prediction of an aircraft's susceptibility to flutter across its intended flight envelope is possible.

Using data from flight tests of the fixed-wing P-FLEX UAV with a 6m wing span, this paper will demonstrate post-flight system identification results and, by extension, ASE model updating using modal parameters identified from Ground Vibration Test. Predictions provided by the updated model regarding flutter boundary will be thoroughly assessed. An additional significant topic is the post-flight verification of the open-loop flutter speed obtained through system identification using flight test data. This is achieved through the monitoring of aeroelastic damping and qualitative comparison of the stability diagrams of the system's poles at different flight speeds. Finally, flutter boundary expansion enabled by the Active Flutter Suppression (AFS) controller of the closed-loop system will be verified via post-flight analysis of the critical flight flutter test data.

1 INTRODUCTION

In consideration of the upcoming critical flutter test, it was essential to ascertain the precision and reliability of the flutter speed predictions derived from updated theoretical model. In order to guarantee a safe flight flutter test a number of flutter calculations have been performed. The structural dynamics modal model was updated by using the eigenfrequencies and damping values that were identified in the Ground Vibration Test (GVT). Further, the GVT-identified modes shapes were taken and mapped to the structural grids of the condensed model. By employing this approach, it is possible to update the structural modal model, which is used directly in the flutter calculations and controller design avoiding to intervene the full Finite Element (FE) Model.

Subcritical and critical flight test data regarding flutter stability analysis of the fixed-wing P-FLEX UAV have been examined via post-flight system identification. For system identification an automatically running robust Stochastic Subspace Identification (rSSI) method is used, which only needs the structural dynamic response data of the aircraft due to non-deterministic natural and/or operational excitations which are provided by atmospheric turbulence and/or pilot control inputs. The outputs of the method are the stochastic system matrices and consequently the flight modal parameters. Flight test identified and predicted flutter speeds derived from the updated model are compared in the context of model validation and clearance for flight flutter testing.

Figure 1: FLiPASED demonstrator aircraft before flight test © DLR 2023

2 FLIPASED DEMONSTRATOR AIRCRAFT

The FLiPASED aircraft (Fig.1) is a jet-powered UAV with a wing span of 7.1 m. It was manually operated within visual line of sight. The demostrator aircraft is equipped with an integrated measurement system [1]. The usual air data, position and inertial parameters are being logged on the aircraft. Attached to the front and rear spars are 12 inertial measurement units (IMU) that records the structural accelerations and angular rates of the wings. The wing-mounted IMUs measure translational accelerations in (x, y, z) direction on the leading edge and translational acceleration z and angular rates (ω_x, ω_y) on the trailing edge resolved in local coordinate system of the sensors. Further, an off-c.g.-mounted IMU at the fuselage provides measured translational accelerations $a_{\text{off-c.g.}} = [a_{x,\text{IMU-fuse}},\, a_{y,\text{IMU-fuse}},\, a_{z,\text{IMU-fuse}}]^T$ and the rotational rates $\Omega_{\text{off-c.g.}} = [p_{\text{IMU-fuse}},\, q_{\text{IMU-fuse}},\, r_{\text{IMU-fuse}}]^T$. A noseboom sensor provides the dynamic pressure, the altitude, the indicated airspeed $V_{\text{IAS, NB}}$, the angle of attack α_{NB} and the angle of sideslip β_{NB}. Figure 2 shows the configuration of the IMUs' placement on the FLiPASED aircraft [2]. The measurement coordinate systems of the sensors are illustrated in Figure 3.

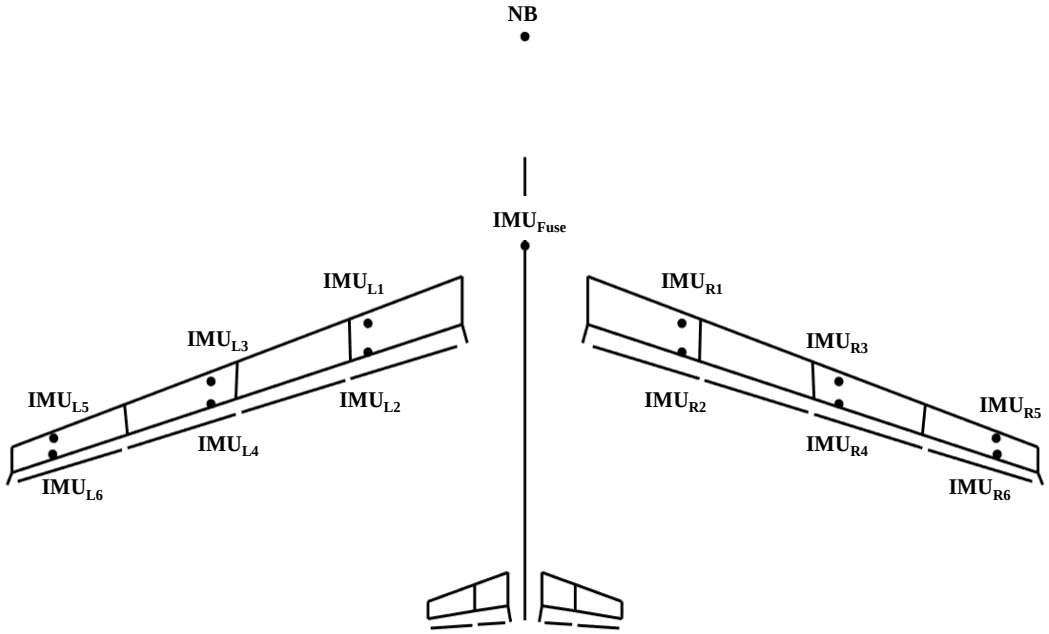

Figure 2: Sensor locations on FLiPASED aircraft [1]

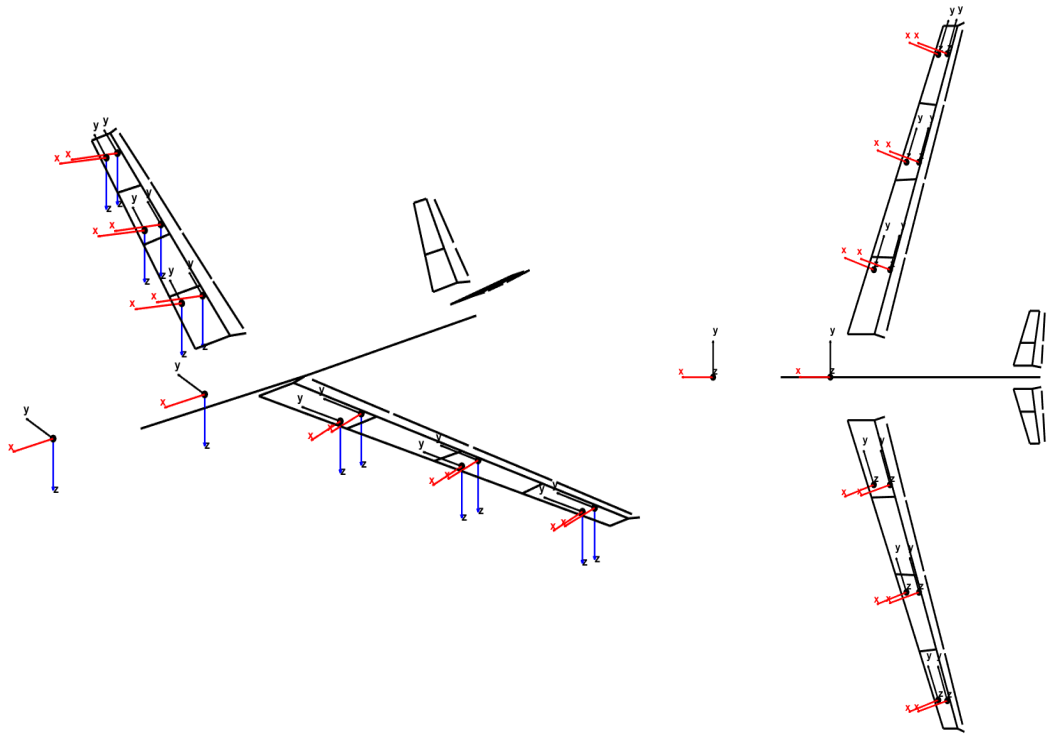

Figure 3: Measurement coordinate systems of the sensors on FLiPASED aircraft [1]

3 NONLINEAR SIMULATION MODEL: THE FLEXIBLE AIRCRAFT

The equations of motion for an unrestrained flexible aircraft can be separated into rigid body motion and elastic body motion, which describe the aircraft's response to external loads such as the aerodynamic and thrust forces. The aircraft rigid body motion is given by the nonlinear Newton-Euler EoM where the aircraft is considered as a rigid body with a constant mass m_b and constant mass moment of inertia $\mathbf{J}_b$:

$$\begin{bmatrix} m_b \left(\dot{V}_b + \Omega_b \times V_b - \mathbf{T}_{bE} g_E \right) \\ \mathbf{J}_b \dot{\Omega}_b + \Omega_b \times (\mathbf{J}_b \Omega_b) \end{bmatrix} = \mathbf{\Phi}_{gb}^T P_g^{\text{ext}}(t) \, , \tag{1}$$

where $V_b = [u \quad v \quad w]^T$ and $\Omega_b = [p \quad q \quad r]^T$ are the translational and angular velocity of the aircraft center of mass with respect to the body frame of reference. The subscript "*b*" denotes "rigib body" part of the motion (*b-set*). The vector $g_E = [0 \quad 0 \quad g]^T$ represents the gravitational acceleration in an earth fixed frame of reference "E" and the matrix $\mathbf{T}_{bE}$ transforms the gravitational vector in "E" to the body fixed frame of reference. In the right hand side of the equation $P_g^{\text{ext}}(t)$ denotes the sum of all nonconservative external loads acting on the aircraft structure. The transpose of the modal matrix $\mathbf{\Phi}_{gb}$ consisting of rigid body modes about the center gravity transformes the load vector $P_g^{\text{ext}}(t)$ into the body frame of reference [4].

For the airframe's elastic motion, linear elastic theory is applied when small perturbations resulting from the airframe's flexibility are assumed. The external loads $P_g^{\text{ext}}(t)$ acting on the structural grids "*g-set*" are dependent on flexible motion, as well as atmospheric disturbances, for example, from discrete gust [5]. The effect of the external loads on the structural dynamics is therefore given by the equations of elastic motion in modal coordinates:

$$\mathbf{M}_{ff}\ddot{u}_f \;+\; \mathbf{B}_{ff}\dot{u}_f \;+\; \mathbf{K}_{ff}u_f \;=\; \mathbf{\Phi}_{gf}^T P_g^{\text{ext}}(t)\;. \tag{2}$$

where $\mathbf{M}_{ff}$ is the modal mass matrix, $\mathbf{B}_{ff}$ is the modal damping matrix and $\mathbf{K}_{ff}$ is the modal stiffness matrix. The subscript "*f*" stands for 'flexible' part of the motion (*f-set*). $u_f, \dot{u}_f, \ddot{u}_f$ are flexible modal deformations, velocities and accelerations respectively. The transpose of the modal matrix $\mathbf{\Phi}_{gf}$ consisting of flexible mode shapes transformes the load vector $P_g^{\text{ext}}(t)$ into the modal form, i.e. into the "*f-set*".

This nonlinear model provides the basis for the derived models for flutter calculations used in this study, which will be detailed upon in subsequent sections.

4 MODEL UPDATING USING MODAL PARAMETER FROM GVT

As mentioned in the beginning the structural dynamics model was updated by using modal parameters, i.e. mode shapes, eigenfrequencies and damping values that were identified in the GVT as listed in the table 1. The experimental modes shapes were taken and mapped to the structural grids of the condensed model, e.g. for the structural grids belonging to the wing structure, the mapping war realized by employing radial basis functions such as the commonly used Infinite Plate Spline [6]. The plots below show the first symmetric wing bending mode identified from GVT (Fig. 4) and its mapped counterpart (Fig. 5). By using this approach, it is possible to update the structural model in modal form, which is used directly in the flutter calculation and controller design avoiding to intervene the full Finite Element (FE) Model. The updated model was then incorporated into the flutter calculation, detailed in the next section, using the *p* method, a classical flutter method. The FLiPASED project deliverable D3.9 [7] contains more details about the GVT procedure and the results that were achieved.

Table 1: Modal parameters obtained from GVT (used for model updating)

Description	**Mode #**	**Eigenfrequency** f [Hz]	**Damping ratio** ζ [%]
2n wing bend-s	6	2.938	1.10
3n wing bend-a	7	7.220	0.79
wing tors-s	9	10.744	0.95
wing tors-a	10	11.155	1.07
4n bending-s	11	12.023	0.72
2n wing inplane-s	13	14.846	1.19
v-tail rock	12	12.501	3.36
5n wing bend-a	17	20.383	1.78
6n wing bend-s	20	25.860	1.82

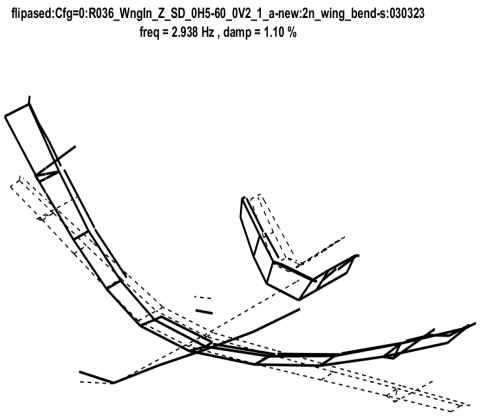

Figure 4: GTV mode (2n wing bend-s)

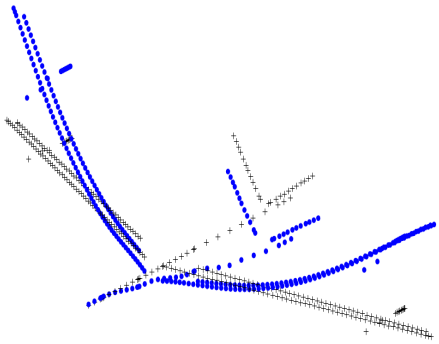

Figure 5: GTV mode mapped to FE model

5 SIMULATION MODEL FOR FLUTTER CALCULATION

This section will introduce the simulation model that is employed for the flutter calculation. Additionally, the flutter equations formulated as a system of first-order ODEs in state-space form, will be derived, which are necessary for the application of the p method. The generalized equations of motion for a linear aeroelastic system in time-domain can expressed in a matrix form as

$$\underbrace{\begin{bmatrix} \mathbf{M}_{bb} & \mathbf{0} \\ \mathbf{0} & \mathbf{M}_{ff} \end{bmatrix}}_{=\mathbf{M}_{hh}} \ddot{u}_h + \underbrace{\begin{bmatrix} \mathbf{0} & \mathbf{0} \\ \mathbf{0} & \mathbf{B}_{ff} \end{bmatrix}}_{=\mathbf{B}_{hh}} \dot{u}_h + \underbrace{\begin{bmatrix} \mathbf{0} & \mathbf{0} \\ \mathbf{0} & \mathbf{K}_{ff} \end{bmatrix}}_{=\mathbf{K}_{hh}} u_h = \frac{1}{2}\rho V^2 \mathbf{Q}_{hh}(\bar{s}, Ma) u_h \tag{3}$$

which describes a system of $n_h = n_b + n_f$ linear ordinary differential equations (ODEs) with n_h generalized degrees of freedom (DoFs) described by $u_h = \begin{bmatrix} u_b \ , \ u_f \end{bmatrix}^T$ where u_b are the rigid-body DoFs consisting of translation of the aircraft's center of mass and rotations of the mean-axis frame with respect to the inertial frame. $\mathbf{M}_{bb}$ is the 6x6 rigib-body mass matrix. Note that the rigid-body and elastic degrees of freedom are inertially decoupled in Eq. 3; however, they are coupled through aerodynamics. Note that other external loads acting on the aircraft structure which are not dependent on the aircraft motion u_h, such as thrust, forces resulting from pilot control inputs or atmospheric disturbances are disregarded on the right hand side of the Eq.3 which are irrelevant for the flutter calculation.

The right hand side of the equation (6) denotes the generalized unsteady aerodynamic forces $P_h^{\text{aero}}(t)$ with

$$P_h^{\text{aero}}(t) = \frac{1}{2}\rho V^2 \mathbf{Q}_{hh}(\bar{s}, Ma) u_h \tag{4}$$

where ρ is the density of atmosphere, V is the true airspeed and $\mathbf{Q}_{hh}(\bar{s}, Ma)$ is the generalized unsteady aerodynamic influence coefficient (AIC) matrix which is a function of the nondimen-

sional Laplace variable $\bar{s}$ and the Mach number Ma. The AIC matrix can be derived by several aerodynamic theories, such as DLM. In this paper, the subsonic unsteady aerodynamic forces have been modeled by means of DLM. Based on small disturbance hypothesis, DLM solves the linearized potential flow equation and obtains the aerodynamic forces under the assumption that aerodynamic surfaces oscillate harmonically. The nondimensional Laplace variable $\bar{s}$ is denoted $\bar{s} = g + ik$ where g is the damping and k is the reduced frequency. On the assumption of harmonic aerodynamic loads the nondimensional Laplace variable $\bar{s}$ becomes:

$$\bar{s} = s\frac{c_{\text{ref}}}{2V} = i\omega\frac{c_{\text{ref}}}{2V} = ik \tag{5}$$

where ω is the frequency of vibration and c_{ref} the reference chord. Note that the dependence on the Mach number of the AIC matrix will be omitted from now on for conciseness.

The generalized AIC matrix $\mathbf{Q}_{hh}(ik) \in \mathbb{C}^{n_h\ x\ n_h}$ in Eq. 3 is a set of matrices which are calculeted for a set of suitable values of reduced frequency k. Thus, in order to compute AIC for any desired reduced frequency and perform time domain analysis (state-space representation), the AIC matrix in the frequency-domain has to be transformed into the Laplace domain and consequently into the time domain. One possible way is to fit the frequency dependent AIC matrix with rational functions in a least-squares sense. This method is called Rational Function Approximation (RFA). In this paper the Roger's formulation [**?**] is used to approximate the AIC matrix $\mathbf{Q}_{hh}(ik)$:

$$\mathbf{Q}_{hh}(ik) = \mathbf{Q}_{hh}(\bar{s}) \ \approx\ \mathbf{Q}_{hh}^0 + \bar{s}\mathbf{Q}_{hh}^1 + \bar{s}^2\mathbf{Q}_{hh}^2 \ +\ \sum_{i=1}^{n_p} \mathbf{Q}_{hh}^{L_i}\frac{\bar{s}}{\bar{s}+\beta_i}. \tag{6}$$

The RFA equation (6) can be interpreted as a general two-part approach for aerodynamic loads based on quasi-steady and lag contributions. $\mathbf{Q}_{hh}^0$, $\mathbf{Q}_{hh}^1$ and $\mathbf{Q}_{hh}^2$ are $\mathbb{R}^{n_h\ x\ n_h}$ real coefficient matrices representing the contribution of acceleration, velocity and displecement of the rigid and flexible degrees of freedom on the aerodynamic loads denoting the quasi-steady part of the approximation. The $\mathbf{Q}_{hh}^{L_i} \in \mathbb{R}^{m\ x\ m}$ matrices with the predefined poles $\beta_i,\ i = 1, 2, ..., n_p$, are responsible for the lagging behavior of the unsteady flow. This is referred to *time lag effect*.

For time domain representation the equation system in (6) can be rearranged as follows [**?**]

$$\mathbf{Q}_{hh}(\bar{s}) \ \approx\ \mathbf{Q}_{hh}^0 + \bar{s}\mathbf{Q}_{hh}^1 + \bar{s}^2\mathbf{Q}_{hh}^2 + \mathbf{D}(\bar{s}\mathbf{I} - \mathbf{R})^{-1}\mathbf{E}\bar{s} \tag{7}$$

where

$$\mathbf{D} = \begin{bmatrix}\mathbf{Q}_{hh}^{L_1} & \mathbf{Q}_{hh}^{L_2} & \dots & \mathbf{Q}_{hh}^{L_{\text{np}}}\end{bmatrix} \in \mathbb{R}^{n_h\ x\ (n_h \cdot n_p)}, \tag{8}$$

$$\mathbf{R} = \ diag\left(\begin{bmatrix}-\beta_1\mathbf{I} & -\beta_2\mathbf{I} & \dots & -\beta_{n_p}\mathbf{I}\end{bmatrix}\right) \in \mathbb{R}^{(n_h \cdot n_p)\ x\ (n_h \cdot n_p)}, \tag{9}$$

$$\mathbf{E} = \begin{bmatrix}\mathbf{I} & \mathbf{I} & \dots & \mathbf{I}\end{bmatrix}^T \in \mathbb{R}^{(n_h \cdot n_p)\ x\ n_h}. \tag{10}$$

For the lag states $x_L \in \mathbb{R}^{n_{lag}\ x\ 1}$ the following ODE with $\dot{u}_h$ as input can be derived [**?**]:

$$\dot{x}_L \ =\ \left(\frac{V}{c_{\text{ref}}/2}\right)\mathbf{R}x_L + \mathbf{E}\dot{u}_h \tag{11}$$

The resulting generalized aerodynamic forces are then

$$\begin{aligned} P_h^{\text{aero}}(t) \ =\ \frac{1}{2}\rho V^2\mathbf{Q}_{hh}(ik)u_h \ \approx\ \frac{1}{2}\rho V^2\Big[&\mathbf{Q}_{hh}^0 u_h + \\ &\frac{c_{\text{ref}}/2}{V}\mathbf{Q}_{hh}^1\dot{u}_h \ +\ \left(\frac{c_{\text{ref}}/2}{V}\right)^2\mathbf{Q}_{hh}^2\ddot{u}_h \ +\ \mathbf{D}x_L\Big] \end{aligned} \tag{12}$$

The equations 4, 5 and 12 can be rearranged in a state-space form parametrized over flight speed V as follows:

$$\begin{bmatrix} \dot{u}_h \\ \ddot{u}_h \\ \dot{x}_L \end{bmatrix} = \mathbf{A}(V) \begin{bmatrix} u_h \\ \dot{u}_h \\ x_L \end{bmatrix} \tag{13}$$

with the system matrix $\mathbf{A}(V)$

$$\mathbf{A}(V) = \begin{bmatrix} \mathbf{0} & \mathbf{I} & \mathbf{0} \\ -(\overline{\mathbf{M}}_{hh})^{-1}\overline{\mathbf{K}}_{hh} & -(\overline{\mathbf{M}}_{hh})^{-1}\overline{\mathbf{B}}_{hh} & \frac{1}{2}\rho V^2(\overline{\mathbf{M}}_{hh})^{-1}\mathbf{D} \\ \mathbf{0} & \mathbf{E} & \frac{2V}{c_{\text{ref}}}\mathbf{R} \end{bmatrix} , \tag{14}$$

where

$$\overline{\mathbf{M}}_{hh} = \mathbf{M}_{hh} - \rho\frac{c_{\text{ref}}^2}{8}\mathbf{Q}_{hh}^2 , \tag{15}$$

$$\overline{\mathbf{B}}_{hh} = \mathbf{B}_{hh} - \frac{c_{\text{ref}}}{4}\rho V\mathbf{Q}_{hh}^1 , \tag{16}$$

$$\overline{\mathbf{K}}_{hh} = \mathbf{K}_{hh} - \frac{1}{2}\rho V^2\mathbf{Q}_{hh}^0 . \tag{17}$$

.

For a given value of the air speed V, the aeroelastic system's modal parameters can be determined using eigenvalue decomposition of the system matrix $\mathbf{A}(V)$ (Eq. 14)

$$\mathbf{A}(V) = \mathbf{\Phi}\mathbf{\Lambda}\mathbf{\Phi}^{-1} \tag{18}$$

where $\mathbf{\Phi}$ is the square $n_h(2+n_p)$ x $n_h(2+n_p)$ matrix whose i^{th} column is the eigenvector ϕ_i of $\mathbf{A}$, and $\mathbf{\Lambda}$ is the diagonal matrix whose diagonal elements are the corresponding eigenvalues (system roots), $\mathbf{\Lambda}_{i,i} = \lambda_i$, with

$$\mathbf{A}(V)\phi_i = \lambda_i\phi_i \tag{19}$$

.

The modal parameters f_i (undamped eigenfrequencies) and ζ_i (damping ratios) can be recovered from the system roots λ_i as follows:

$$\lambda_i = -\zeta_i\omega_i + i\omega_i\sqrt{1-\zeta_i^2} \;\Rightarrow\; f_i = \frac{|\lambda_i|}{2\pi} \;,\; \zeta_i = -\frac{\mathfrak{Re}(\lambda_i)}{|\lambda_i|}. \tag{20}$$

This method of solving the flutter equation formulated as a first order ODE in a state-space form (Eq. 13), where the roots of the system matrix can be determined directly, will be called the p method (transient method) [8]. In this study the p method was employed for the determination of the flutter results for the simulation model.

6 POST-FLIGHT SYSTEM IDENTIFICATION RESULTS

In the context of model validation and clearance for flight flutter testing, identified and predicted flutter speeds derived from the updated model are compared. A post-flight system identification employing non-critical flight test data from FT32 was used for obtaining the experimental prediction of the open-loop flutter speed and the validation of the updated simualtion model. For the post-flight system identification an automatically running robust Stochastic Subspace Identification (rSSI) method is used, which only requires structural responses of the aircraft due to non-deterministic natural excitations which are provided by atmospheric turbulence. The outputs of the method are the stochastic system matrices and consequently the flight modal parameters.

6.1 Post-flight system identification for non-critical flight test below open-loop flutter speed

Firstly, the non-critical flight test data from FT32 was used for the experimental prediction of the open-loop flutter speed. This flight was performed using constant bank angle circles with a radius of 800m at an altitude (ALT) of ca. 360 m and with an engaged autopilot keeping the speed as constant as possible. The flight speed was increased incrementally increased from 44 m/s to 54 m/s. An output-only Operational Modal Analysis tool was implemented on a secondary flight computer onboard to closely track online the flight modal parameters during the flight test. The online modal analysis system is detailed in [9].

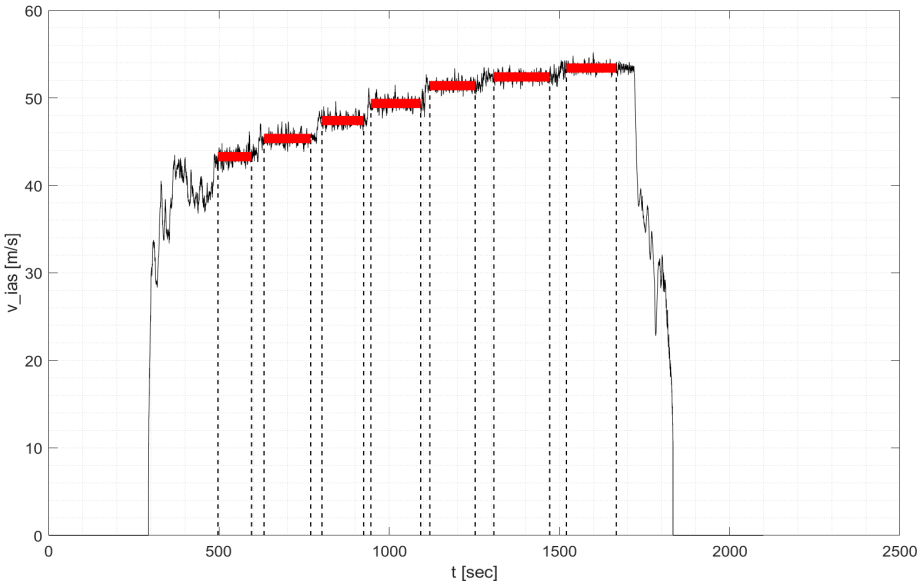

Figure 6: Flight speed profile FT32

Figure 7 demonstrates post-flight system identification results with respect to identified aeroelastic eigenfrequencies and damping ratios for the flight points at 44, 46, 48, 50, 52, 53, and 54 m/s compared with their counterparts computed from GVT verified simulation model. An excellent correlation of the flight modal parameters between model and flight test data has been achieved. The damping evolution of the critical flutter mode (1st symmetric wing torsion) is particularly well captured, which confirms the expected open-loop flutter speed at approximately 55 m/s, or more precisely 55.2 m/s (flight test data) and 55.4 m/s (updated model).

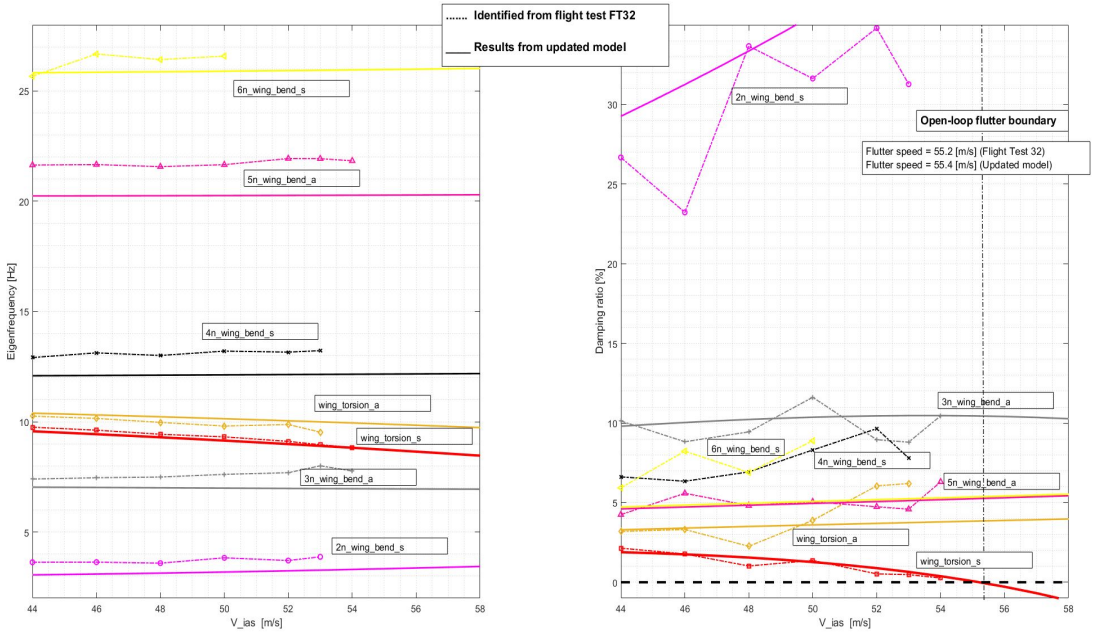

Figure 7: Comparison of flight modal parameters obtained from updated model and identifed from FT32

The flutter mode becomes dominant as the flight speed approaches the flutter speed, and the damping decreases to nearly zero. Other modes become more challenging to track, and in this case, they disappear, at least from the standpoint of theory. This phenomenon can be detected by analyzing both the sum of output spectra of the measured responses and stabilization diagram within modal identification. This is consistent with the results in [2], published in 2019, which demonstrated this effect using simulated test data as illustrated in the figure 8 where only the dominant flutter mode can be identified at the critical flutter speed.

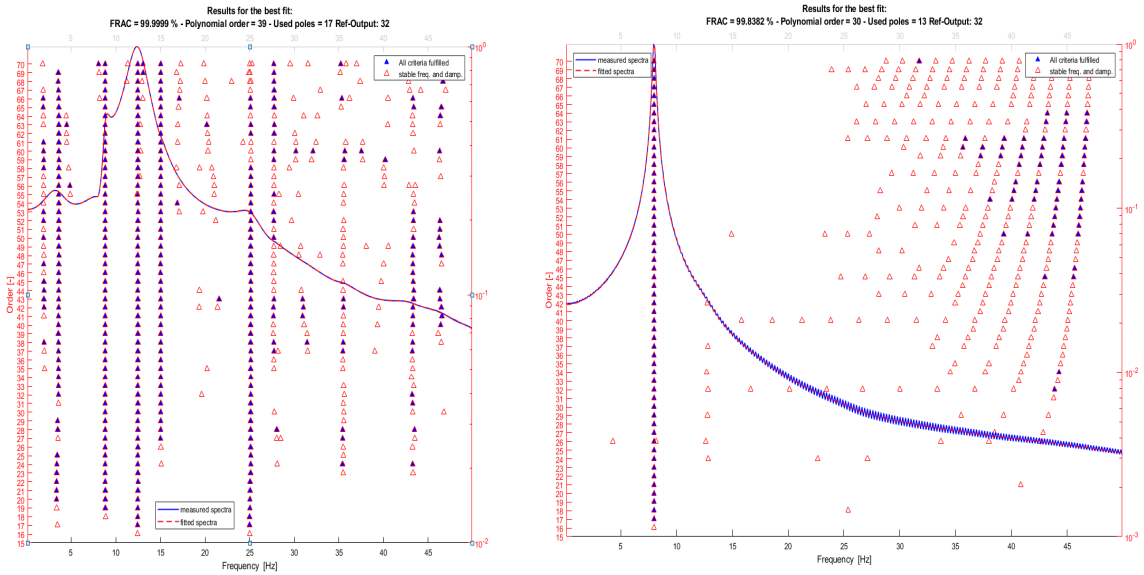

Figure 8: *Uncleaned* stabilization diagrams at noncritical flight speed (left) and at flutter speed (right) obtained through simulated flight test data from the study in [2]

Analogous results have been achieved for the subcritical flight test FT32 shown in the subsequent figure 9. Only the dominant flutter mode (symmetric wing-tors. $f_{flut} = 8.7$ Hz) is clearly visible (”one-peak”) on the output spectra (blue graph) at nearly flutter speed of $v = 54$ m/s which progressively start to become unstable as already confirmed through damping evolution results.

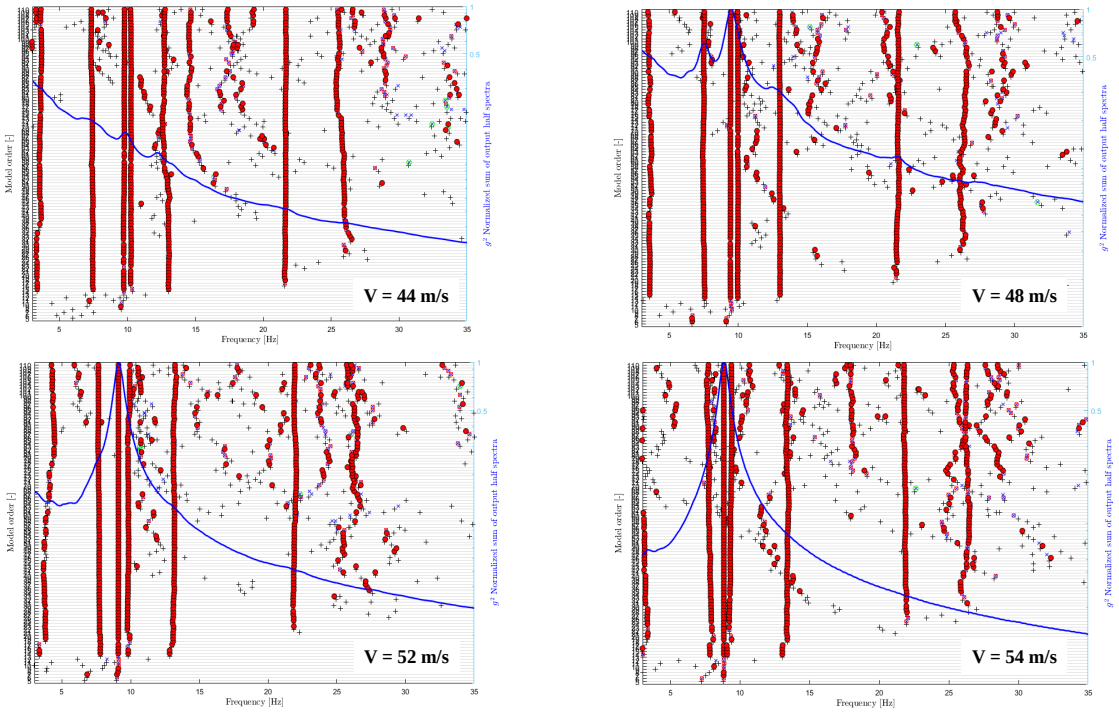

Figure 9: *Uncleaned* stabilization diagrams for different flight speeds obtained from post-flight system identification (FT32)

6.2 Post-flight system identification for critical flight test beyond open-loop flutter speed

The objective of FT35 was to assess the system’s performance at critical flutter velocities. Finally, flutter boundary expansion enabled by the AFS controller of the closed-loop system has been confirmed via post-flight modal identification. Here the flight modal damping parameters identified from FT32 (open-loop) and those extracted from FT35 (closed-loop with AFS controller ON at flight points 50, 52, 54, 55, 56, 57, and 58 m/s) are compared. The results are visualized in the figures 10 and 11.

From the plots shown in Fig. 10, it is evident that activating the AFS controller increases the damping of the critical flutter mode (1st wing torsion), hence allowing the aircraft to operate at speeds beyond its open-loop flutter speed. The stability diagrams obtained from FT35 can also be used to confirm flutter stability, as they indicate that none of the eigenmodes, particularly the first torsion mode, become dominant, resulting in an *one-peak* in the output spectra plot.

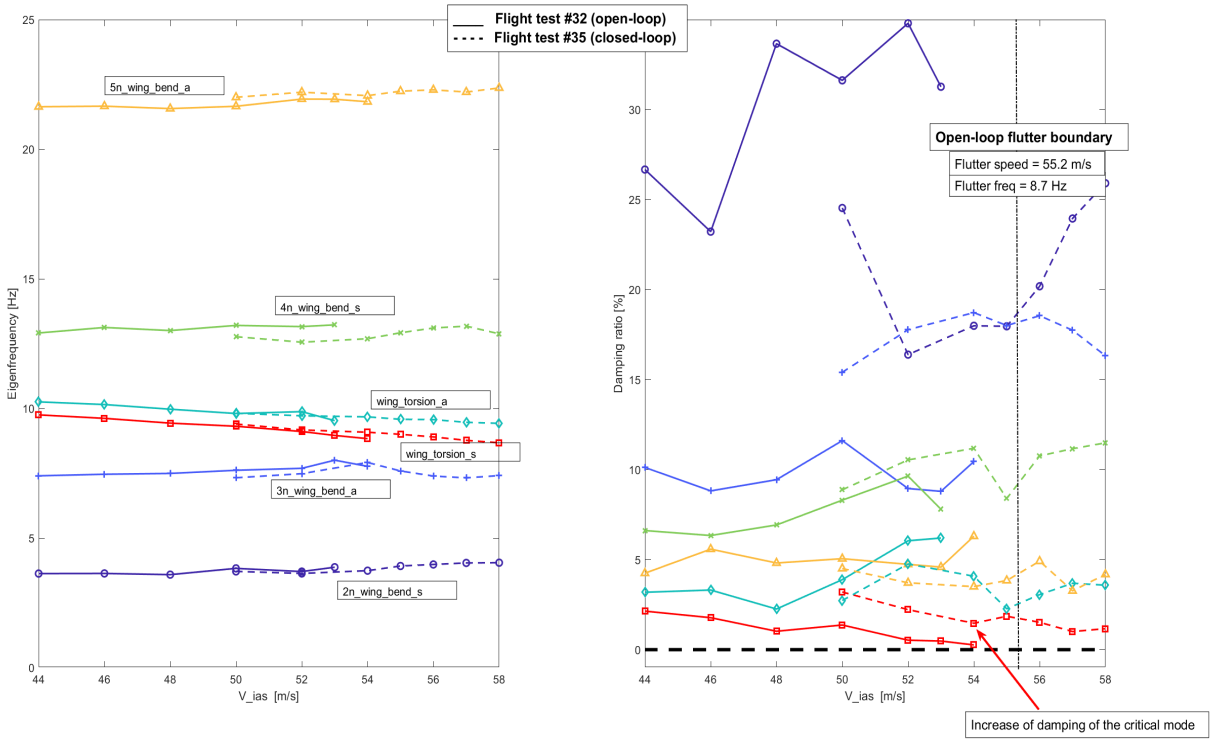

Figure 10: Comparison of flight modal parameters obtained from FT32 (open-loop) and FT35 (closed-loop)

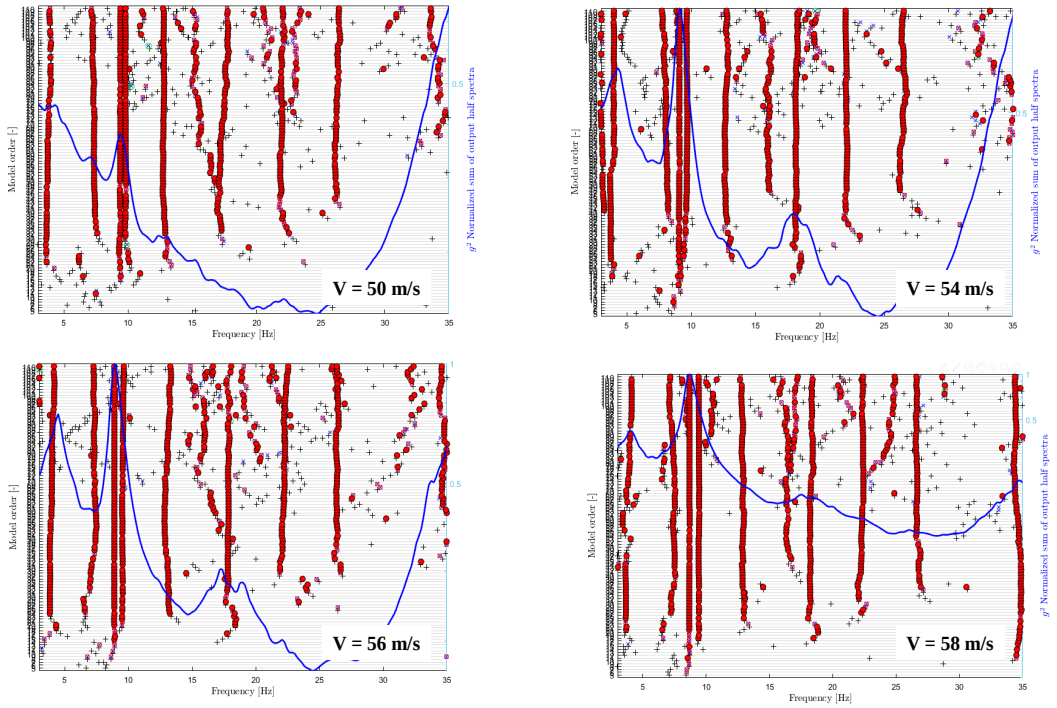

Figure 11: *Uncleaned* stabilization diagrams for different flight speeds obtained from post-flight system identification of the critical flight test FT35

7 CONCLUSION

In this study, post-flight system identification results and predictions provided by the updated model regarding flutter boundary have been thoroughly assessed. The open-loop flutter speed has been successfully verified through post-flight modal identification. This is achieved through monitoring of aeroelastic damping and additionally qualitative comparison of the stability diagrams of the system's poles at different flight speeds. Finally, flutter boundary expansion enabled by the AFS controller of the closed-loop system has been verified via post-flight analysis employing critical flight test data.

8 REFERENCES

[1] Süelözgen, Ö. (2023). Application and validation of a model updating approach for linearized state-space models of flexible aircrafts using multiple flight test data. *AIAA SCITECH 2023 Forum*. doi:10.2514/6.2023-0374.

[2] Süelözgen, Ö. and Wüstenhagen, M. (2019). Operational modal analysis for simulated flight flutter test of an unconventional aircraft. *IFASD, The International Forum on Aeroelasticity and Structural Dynamics, 9-13 June 2019, Savannah, Georgia, USA*.

[3] Wüstenhagen, M., Süelözgen, Ö., Ackermann, L., et al. (2021). Validation and update of an aeroservoelastic model based on flight test data. *IEEE Aerospace Conference*.

[4] Kier, T. M. and Looye, G. H. N. (2009). Unifying manoeuvre and gust loads analysis models. *IFASD, The International Forum on Aeroelasticity and Structural Dynamics 2009, Seattle, WA*.

[5] Süelözgen, Ö. (2022). A novel updating algorithm for linearized state-space models of an unmanned flexible aircraft using flight test data. *AIAA SCITECH 2022 Forum*. doi: 10.2514/6.2022-0725.

[6] Harder, R. and Desmarais, R. (1972). Interpolation using surface splines. In *Journal of Aircraft, 9(2)*. pp. 189–191. doi:10.2514/3.44330.

[7] Yu, F., Teubl, D., Toth, S., et al. (2024). Advanced wing integration and ground test. In *Tech. Rep. D 3.9, FliPASED*.

[8] Abel, I. (1979). An analytical technique for predicting the characteristics of a flexible wing equipped with an active flutter-suppression system and comparison with wind-tunnel data.

[9] Soal, K., Volkmar, R., Thiem, C., et al. (2023). Flight vibration testing of the t-flex uav using online modal analysis. In *In AIAA SCITECH 2023 Forum, American Institute of Aeronautics and Astronautics*. doi:10.2514/6.2023-0373.

COPYRIGHT STATEMENT